CrystEngComm

ROYAL SOCIETY OF CHEMISTRY

PAPER

View Article Online
View Journal | View Issue

Cite this: *CrystEngComm*, 2025, **27**, 30

Chiral-driven formation of hybrid cyanurates with large birefringence†

Yue Zhao,[abc] Chun-Li Hu,[a] Peng-Fei Chen,[abc] Ming-Zhi Zhang[ac] and Jiang-Gao Mao *[abc]

Ultraviolet (UV) birefringent crystals have important applications in polarizers, optical isolators and optical information processing. Crystals with large birefringence can enhance the modulation ability of light and realize the miniaturization of devices. However, the birefringence of cyanurates is often limited by the large dihedral angles between anionic groups. In this work, a chiral-driven approach is proposed for the first time to construct cyanurates with large birefringence. We combined racemic or chiral α-methylbenzylamine (α-MBA) molecules with a π-conjugated cyanurate group (CY), which led to the isolation of three organic hybrid cyanurates with wide band gaps >5.10 eV, namely, *rac*-α-MBACY, *R*-α-MBACY, and *S*-α-MBACY. Notably, the presence of chirality leads to a significant reduction of the dihedral angle between the α-MBA cation and $(H_2C_3N_3O_3)^-$ anion and a threefold increase in birefringence from 0.113@546 nm to 0.344@546 nm and 0.338@546 nm. The birefringence values of *R*-α-MBACY and *S*-α-MBACY exceed those of most of the cyanurates and commercial crystals, indicating their potential as UV birefringent crystals. This work provides new insights into the design and syntheses of UV birefringent materials.

Received 5th November 2024,
Accepted 18th November 2024

DOI: 10.1039/d4ce01123f

rsc.li/crystengcomm

Introduction

Ultraviolet (UV) birefringent crystals are an important class of optoelectronic functional materials, which have a wide range of applications in polarization devices, optical isolators and polarimetric information processing.[1–8] The commercially available birefringent crystals include α-BaB_2O_4 (Δn = 0.116@1064 nm), MgF_2 (Δn = 0.012@400 nm), YVO4 (Δn = 0.208@1064 nm) and $CaCO_3$ (Δn = 0.172@1064 nm).[9,10] However, their practical applications are limited by their own defects, such as phase transition and high anisotropy thermal expansion problems for α-BaB_2O_4,[9] an extremely small birefringence index for MgF_2,[10] a narrow transmission range for YVO_4 (ref. 11) and the difficulty to grow high-quality large single crystals for $CaCO_3$.[12] Therefore, it is still of great research significance to design and synthesize new birefringent crystals with excellent optical properties.

The birefringence property of crystals is closely related to the types and arrangements of their functional groups. To improve the birefringence, a common means is to introduce distorted polyhedra of metal cations (Pb^{2+}, Sn^{2+}, Bi^{3+}, Sb^{3+}, *etc.*) with stereochemically active lone pairs to enlarge the optical anisotropy;[13–18] however, this strategy is not suitable for UV birefringent crystals because these cations are prone to form materials with narrow band gaps. The current research studies on the design of UV birefringent crystals mainly focus on the strategy of introducing π-conjugated groups with large optical anisotropy, such as $(NO_3)^-$, $(CO_3)^{2-}$, $(BO_3)^{3-}$, $(B_3O_6)^{3-}$, $(H_xC_3N_3O_3)^{x-3}$, *etc.*[19–32] The excellent performance of the well-known commercial birefringent crystal α-BBO originated from $(B_3O_6)^{3-}$ functional groups. Notably, $(H_xC_3N_3O_3)^{x-3}$ groups have a planar π-conjugated structure similar to $(B_3O_6)^{3-}$ groups and possess stronger conjugation, which is beneficial to induce larger birefringence.[33,34] In fact, most of the reported cyanurates exhibit good birefringence with a wide UV transmission band, such as $KLi(HC_3N_3O_3)\cdot 2H_2O$ (E_g = 5.23 eV and Δn = 0.186@514 nm),[30] $Rb(H_3C_3N_3O_3)(NO_3)$ (E_g = 4.98 eV and Δn = 0.224@546.1 nm)[35] and $Cs_3Na(H_2C_3N_3O_3)_4\cdot 3H_2O$ (E_g = 5.46 eV and Δn = 0.29@514 nm).[36] However, in many crystals, the orientation of cyanurate groups is not always aligned,[29] as those in $RbBr(H_3C_3N_3O_3)_2$ with a large dihedral angle between adjacent cyanurate groups close to 87.9°, leading to a small birefringence of 0.075@800 nm.[37] Therefore, it is of great value to explore new methods for regulating the orientations of cyanurate groups.

In recent years, chiral organic cations have emerged as promising candidate groups for second-order nonlinear

[a] *State Key Laboratory of Structural Chemistry, Fujian Institute of Research on the Structure of Matter, Chinese Academy of Sciences, Fuzhou 350002, P. R. China. E-mail: mjg@fjirsm.ac.cn*
[b] *School of Physical Science and Technology, ShanghaiTech University, Shanghai 201210, P. R. China*
[c] *University of Chinese Academy of Sciences, Beijing 100049, P. R. China*

† Electronic supplementary information (ESI) available. CCDC 2349919–2349921. For ESI and crystallographic data in CIF or other electronic format see DOI: https://doi.org/10.1039/d4ce01123f

optics and spintronic devices due to their high possibility to form chiral structures.[38–47] For example, Zou and Lin obtained (L-ipp)(L-pro)PbI_3 with a SHG intensity of up to 8× KH_2PO_4 (KDP) by using an *in situ* chiral templating method.[42] Xu *et al.* proposed a resonant pathway from metal halide polyhedra to the charge-transfer excited states of chiral organic ligands and obtained $(C_7H_{10}N)PbBr_3$ with over 111× KDP frequency doubling intensity.[45] In contrast to their wide applications in nonlinear optical materials, chiral organic cations received less research attention in the field of birefringence. However, the high birefringence exhibited by certain compounds, such as *R*/*S*-$[(C_8H_{10}NO_3)_2]Sn(IV)F_6$ (0.328@546.1 nm),[48] has drawn attention to the potential applications of these chiral organic cations. Considering the helical arrangement of chiral cations in some metal halides,[45,49–51] partially π-conjugated chiral cations may have the potential to modulate the dihedral angles between π-conjugated groups and thus adjust the birefringence.

In this work, different isomers of the α-methylbenzylamine (α-MBA) molecule were introduced into the cyanurate system, which led to the isolation of three novel metal-free cyanurates, namely, (*rac*-α-$C_8H_{12}N$)($H_2C_3N_3O_3$) (*rac*-α-MBACY), (*R*-α-$C_8H_{12}N$)($H_2C_3N_3O_3$) (*R*-α-MBACY) and (*S*-α-$C_8H_{12}N$)($H_2C_3N_3O_3$) (*S*-α-MBACY). The presence of chirality induces a decrease of the dihedral angle between the α-MBA cation and $(H_2C_3N_3O_3)^-$ anion and a large increase in the birefringence from 0.113@546 nm for *rac*-α-MBACY to 0.344@546 nm for *R*-α-MBACY and 0.338@546 nm for *S*-α-MBACY. In addition, all three compounds have large band gaps. Herein, we report their syntheses, crystal structures and optical properties.

Experimental section

Reagents

$H_3C_3N_3O_3$ (Aladdin ≥99.0%), NaCl (Adamas 99.999%), (*R*)-(−)-alpha-methylbenzylamine (Adamas, ≥99.0%) and (*S*)-(+)-alpha-methylbenzylamine (Adamas, ≥99.0%) were used as received without further purification.

Syntheses

Single crystals of *rac*-α-MBACY, *R*-α-MBACY and *S*-α-MBACY were synthesized by hydrothermal methods. With NaCl (0.058 g, 1 mmol) as the mineralizer, an equal mixture of (*R*)-(−)-alpha-methylbenzylamine and (*S*)-(+)-alpha-methylbenzylamine (0.5 mL)/(*R*)-(−)-alpha-methylbenzylamine (0.5 mL, 3.9 mmol)/(*S*)-(+)-alpha-methylbenzylamine (0.5 mL, 3.9 mmol) was added to 5 mL deionized water containing $H_3C_3N_3O_3$ (0.129 g, 0.5 mmol), respectively. Then, the resultant mixture was transferred to a 23 mL Teflon autoclave and heated to 90 °C within 1 h, kept at 90 °C for 5 days, and finally cooled down naturally to room temperature. After filtration, colourless prismatic crystals of *rac*-α-MBACY, *R*-α-MBACY and *S*-α-MBACY were collected in a yield of 40%, 60% and 50% (based on $H_3C_3N_3O_3$), respectively. As shown in Fig. S2,† the powder XRD patterns of all compounds match with the calculated ones, proving that the pure phases were obtained.

Single-crystal structure determination

X-ray diffraction data of *rac*-α-MBACY, *R*-α-MBACY and *S*-α-MBACY were collected on a Rigaku Oxford Diffraction XtaLAB Synergy-R diffractometer at 293 K using a graphite monochromatic Cu Kα radiation source (λ = 1.54184 Å). Data reductions were performed using CrysAlisPro software and the absorption corrections were applied using a multi-scan approach. The three structures were determined by direct methods using Olex2-1.5 software as a graphical interface, the ShelXT 2018/2 program as a solution program and refined with the ShelXL 2018/3 program by full-matrix least-squares fitting on F^2.[52–54] All non-hydrogen atoms were refined with anisotropic thermal parameters. All of the hydrogen atoms associated with organic cations and cyanurates were placed at the geometrically calculated positions and refined with isotropic thermal parameters. The program PLATON was used to check for possible missing symmetries in all compounds, but none were found.[55] The crystal data and structural refinement information for all compounds are summarized in Table 1, and the atomic coordinates and equivalent isotropic displacement parameters, selected bond lengths, and hydrogen bonds are listed in Tables S1–S3.†

Powder X-ray diffraction

Powder X-ray diffraction (PXRD) patterns of all three samples were collected in the 2θ range of 5–60° using a Rigaku Miniflex 600 X-ray diffractometer with graphite-monochromate Cu Kα radiation (λ = 1.54186 Å).

Thermal analysis

Thermogravimetric analyses (TGA) were performed on a NETZCH STA 449F3 thermal analyser under a nitrogen atmosphere in the temperature range of 293–800 K at a heating rate of 15 K min^{-1}.

Spectroscopic measurements

Infrared (IR) spectra with a resolution of 2 cm^{-1} were obtained in the range of 4000–400 cm^{-1} using a Nicolet Magna 750 FT-IR spectrometer with air as the background. UV-vis-NIR spectra were acquired in the 200 to 1500 nm range utilizing a PerkinElmer Lambda 950 UV-vis-NIR spectrophotometer, with $BaSO_4$ serving as the 100% reflectance reference.

Birefringence measurements

The birefringence of *rac*-α-MBACY and *R*-α-MBACY was assessed using a Zeiss Axio A1 polarizing microscope equipped with a Berek compensator, under a light source at λ = 546 nm. The formula for calculating the birefringence Δn

Table 1 Crystal data and structure refinements for *rac*-α-MBACY, *R*-α-MBACY and *S*-α-MBACY

	rac-α-MBACY	*R*-α-MBACY	*S*-α-MBACY
Formula	$C_{11}H_{14}N_4O_3$	$C_{11}H_{14}N_4O_3$	$C_{11}H_{14}N_4O_3$
Formula weight	250.26	250.26	250.26
Temperature/K	293(2)	293(2)	293(2)
Crystal system	Monoclinic	Monoclinic	Monoclinic
Space group	$P2_1/c$	$P2_1$	$P2_1$
a/Å	15.9636(3)	7.84010(10)	7.84020(10)
b/Å	6.64630(10)	12.40940(10)	12.41110(10)
c/Å	11.5269(2)	12.46850(10)	12.47300(10)
α/°	90	90	90
β/°	98.410(2)	96.7100(10)	96.7460(10)
γ/°	90	90	90
Volume/Å^3	1209.84(4)	1204.76(2)	1205.29(2)
Z	4	4	4
D_c (g cm^3)	1.374	1.38	1.379
μ/mm^{-1}	0.86	0.864	0.864
λ/Å	Cu Kα	Cu Kα	Cu Kα
GOF on F^2	1.066	1.049	1.056
Flack factor	None	−0.03(15)	−0.01(7)
R_1, wR_2 [$I > 2\sigma(I)$]	0.0380, 0.1038	0.0388, 0.1042	0.0329, 0.0907
R_1, wR_2 (all data)	0.0437, 0.1089	0.0416, 0.1070	0.0336, 0.0915

$R_1 = \sum||F_o| - |F_c||/\sum|F_o|$ and $wR_2 = \{\sum[w(F_o^2 - F_c^2)^2]/\sum[wF_o^2]^2\}^{1/2}$.

is: $R = \Delta n \times d$ (R represents the optical path difference and d represents the thickness).

Second-harmonic generation measurements

Second-harmonic generation (SHG) measurements of *R*-α-MBACY and *S*-α-MBACY were conducted utilizing a Q-switched Nd:YAG laser with a wavelength of 1064 nm, employing the Kurtz and Perry method.[56] The particle size of the samples ranged from 70 to 100 mesh, with KDP samples of equivalent particle sizes selected as reference points.

Computational description

The electronic structure and optical properties of all three compounds were calculated by the first-principles plane wave pseudopotential method with density functional theory (DFT) and GGA-PBE exchange–correlation functional, which were implemented by the total energy code CASTEP.[57–59] The interaction between nuclei and electrons was described by norm conservation pseudopotentials.[60] The selection of plane-wave basis sets for the three compounds was dictated by a cutoff energy of 750 eV and a Monkhorst–Pack k-point sampling of 4 × 4 × 2. The calculations considered the C-2s^{2}2p^2, N-2s^{2}2p^3, O-2s^{2}2p^4, and H-1s^1 orbital electrons as the valence electrons. The electronic band structure underwent the scissor correction, while the imaginary part of the dielectric function was determined by electron transitions from the valence band (VB) to the conduction band (CB). The real part of the dielectric function was obtained through the Kramers–Kronig transformation. Subsequently, the refractive index was derived, and the birefringence Δn was calculated as the difference between the maximum and minimum refractive indices. The default values of the CASTEP code were employed for all other calculation parameters and convergence criteria.

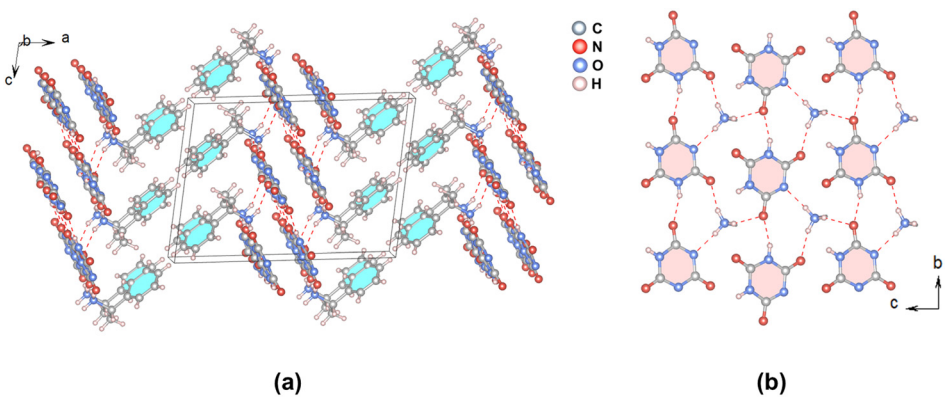

Fig. 1 View of the crystal structure of *rac*-α-MBACY down the *b* axis (a) and a single hydrogen-bonded layer in *rac*-α-MBACY (b). Hydrogen bonds are drawn as dashed lines.

Results and discussion

Crystal structure descriptions

rac-α-MBACY crystallizes in the centrosymmetric monoclinic space group $P2_1/c$ (no. 14), and it shows obvious double hydrogen-bonded layer characteristics (Fig. 1a). Its asymmetric unit consists of a *R*-α-MBA cation and a $(H_2C_3N_3O_3)^-$ group, which forms a $[(R\text{-}\alpha\text{-}C_8H_{12}N)(S\text{-}\alpha\text{-}C_8H_{12}N)(H_2C_3N_3O_3)_2]$ dimeric unit under the symmetry operation of the *c* glide plane. The α-MBA cation exhibits a dihedral angle of 73.896° relative to the $(H_2C_3N_3O_3)^-$ group; hence, they are not aligned. The lengths of C–O, C–N, and C–C bonds in the structure are 1.2216(15)–1.2436(14) Å, 1.3407(14)–1.4978(16) Å, and 1.359(3)–1.520(2) Å, respectively, all within the reasonable bond length range.

The NH_3 groups of the α-$C_8H_{12}N$ cations and cyanurate anions are interconnected *via* hydrogen bonds (N–H···N and N–H···O) (Table S3†), forming a 2D layer in the *bc*-plane (Fig. 1b), and two such layers are further held together *via* hydrogen bonds into a thick double layer (Fig. S3†) with the organic rings of the cations hanging on both sides of the double layer. The neighboring aromatic rings are at least 4.0 Å away from each other; hence, their π–π stacking interactions are expected to be weak. These 2D layers are held together by van der Waals interactions into a 3D supramolecular structure (Fig. 1a).

Both *R*-α-MBACY and *S*-α-MBACY crystallize in the non-centrosymmetric (NCS) monoclinic space group $P2_1$ (no. 4). Considering the similarity of *R*-α-MBACY and *S*-α-MBACY structures, only the structure of *R*-α-MBACY is described as a representative. The basic structural unit of *R*-α-MBACY consists of two unique *R*-α-MBA chiral cations and two unique $(H_2C_3N_3O_3)^-$ groups, which are interconnected by the hydrogen bonds (N(7)–H(7A)···N(3), N(7)–H(7B)···O(6), N(8)–H(8A)···O(3), and N(8)–H(8B)···O(6) Table S3†) to form a 2D layer parallel to the $(10\bar{1})$ plane (Fig. 2b) with the organic groups of the *R*-α-MBA hanging on both sides of the layer. The bond lengths of C–O, C–N, and C–C are 1.229(3)–1.251(3) Å, 1.333(4)–1.499(4) Å, and 1.338(9)–1.514(5) Å, respectively. These values are close to those in *rac*-α-MBACY.

The two different *R*-α-MBA cations are not coplanar but exhibit a dihedral angle in the range of 4.9–16.9°, and the dihedral angle between the two unique cyanurate anions is in the range of 9.2–19.8°; hence, they are also not well-aligned. The dihedral angles between *R*-α-MBA cations and cyanurate anions are in the range of 11.4–26.2°, being much smaller than those in *rac*-α-MBACY, which is favourable to generate a larger birefringence. Furthermore, there exists π–π stacking interactions between *R*-α-MBA cations and $(H_2C_3N_3O_3)^-$ groups with the shortest inter-ring distance of 3.717 Å. Hence, these hydrogen-bonded 2D layers are held together by π–π stacking interactions and van der Waals forces into a 3D super-molecular network (Fig. 2a). In Fig. 3, a similar helical arrangement of α-MBA cations along the $(H_2C_3N_3O_3)^-$ chains can be observed as in some chiral metal halides.[45,49–51]

It is interesting to note that the chiral organic amine plays an important role in the arrangements of the organic amine and cyanurate anions and the optical properties of the materials formed. The protonated chiral organic amine acts as the structural direct agent. *rac*-α-MBACY, *R*-α-MBACY, and *S*-α-MBACY were isolated under similar reaction conditions except for the different chiralities of the organic amine. When racemic α-MBA was used, the material isolated *rac*-α-MBACY is structurally centrosymmetric, and the amine groups of the α-MBA and cyanurate anions formed a hydrogen-bonded 2D layer in which the organic rings are almost perpendicular to the 2D layer; hence, the α-MBA and CY groups are not coplanar and unable to produce a large anisotropy. Therefore, it is expected that *rac*-α-MBACY will display a small birefringence. When only *R*-α-MBA or *S*-α-MBA was used, the materials formed *R*-α-MBACY and *S*-α-MBACY are chiral, and the amine groups of α-MBA and cyanurate anions also form a hydrogen bonded 2D layer. However, the organic rings of the α-MBA form a much smaller dihedral angle with cyanurate groups, and hence,

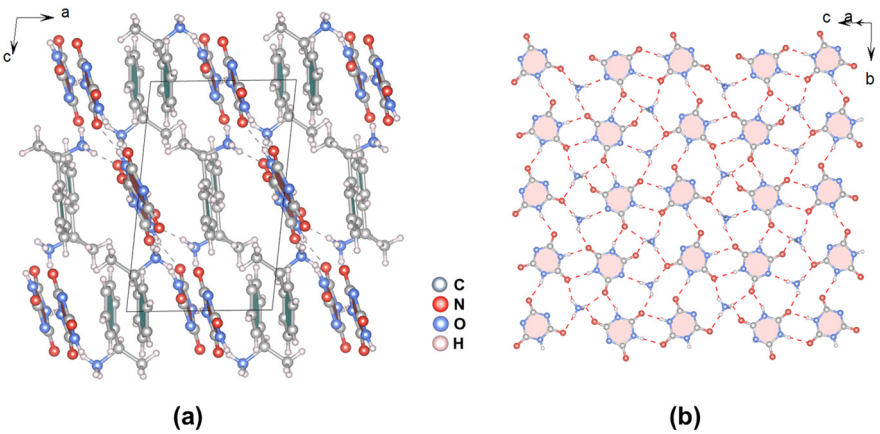

Fig. 2 View of the crystal structure of *R*-α-MBACY down the *b* axis (a) and a hydrogen-bonded layer formed by the –NH_3 groups of the *R*-α-MBA and cyanurate anions parallel to the $(10\bar{1})$ plane (b). Hydrogen bonds are drawn as dashed lines.

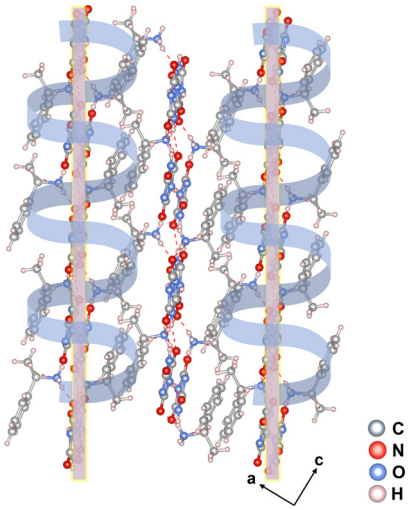

Fig. 3 Schematic diagram of the helical arrangement of α-MBA around the $(H_2C_3N_3O_3)^-$ chains in *R*-α-MBACY.

both kinds of organic groups are able to produce a large anisotropy; hence, the birefringence values of *R*-α-MBACY and *S*-α-MBACY are expected to be much larger than that of *rac*-α-MBACY, as will be confirmed by our experimental measurements, which will be discussed later.

Thermal analysis

As thermodynamic properties are independent of the compound's configuration, we conducted thermogravimetric analysis (TGA) on *rac*-α-MBACY and *R*-α-MBACY. The results showed that *rac*-α-MBACY and *R*-α-MBACY exhibited the same thermal stability and thermal behaviour under a N_2 atmosphere (Fig. S4†), and they are stable up to 392 K and 396 K, respectively. Then, both of them experienced two main mass loss steps. The first mass losses are 47.8% (cal. 48.4%) and 48.3% (cal. 48.4%) in the range of 392–456 K and 396–459 K, corresponding to the release of the α-MBA groups, and the second mass losses are 51.1% (cal. 51.6%) and 51.3% (cal. 51.6%) in the temperature ranges of 563–663 K and 571–679 K, which can be attributed to the decomposition of the $(H_2C_3N_3O_3)^-$ groups. The decomposition temperature of the $(H_2C_3N_3O_3)^-$ groups coincides with that of cyanuric acid.

IR and UV-vis-NIR spectra

As shown in Fig. S5,† *rac*-α-MBACY, *R*-α-MBACY and *S*-α-MBACY showed similar IR fingerprints. The absorption peaks in the range of 900–400 cm^{-1} can be attributed to the overlap of the bending vibration of the $(H_2C_3N_3O_3)^-$ group with the benzene ring, while the absorption peaks in the range oft 1400–900 cm^{-1} are due to the stretching vibration of C–N bonds and the bending vibration of the N–H bond and C–H bond. The absorption peaks in the range of 1750–1400 cm^{-1} can be attributed to the overlap of the stretching vibration of $(H_2C_3N_3O_3)^-$ and the bending vibration of the N–H bond of α-MBA; besides, the absorption peaks in the range from 3200 to 2900 cm^{-1} were assigned to the stretching vibrations of N–H, C–H and hydrogen bonds. The assignment of these vibrational peaks is basically consistent with those reported for compounds.[31,61–65]

The UV-vis-NIR diffuse reflectance spectra of all three compounds were measured, and the results are shown in Fig. 4. It can be seen that the band gaps of the three compounds are 5.34 eV, 5.12 eV and 5.25 eV, and the corresponding ultraviolet cut-off edges are 214 nm, 212 nm and 220 nm, which indicate that they all have high transmittance in the ultraviolet waveband. Notably, the band gaps of the three compounds are comparable to most of the alkali metal and alkaline earth metal cyanurates reported, such as $KLi(HC_3N_3O_3)\cdot 2H_2O$ (5.23 eV),[30] $Rb(H_3C_3N_3O_3)(NO_3)$ (4.98 eV)[35] and $Cs_3Na(H_2C_3N_3O_3)_4\cdot 3H_2O$ (5.46 eV).[36] This verifies that organic cations may have a positive role in the band gap elevation of cyanurates as in alkali and alkaline earth metals.

Second-harmonic generation measurements

R-α-MBACY and *S*-α-MBACY crystallized in the NCS $P2_1$ (no. 4) space group. Both crystals exhibited SHG signals of 0.2× KDP at 1064 nm laser irradiation with a particle size range of 70–100 mesh (Fig. S6†), which indicated that the presence of chiral cations in the cyanurates is very likely to form materials with chiral and NCS structures. Notably, *R*-α-

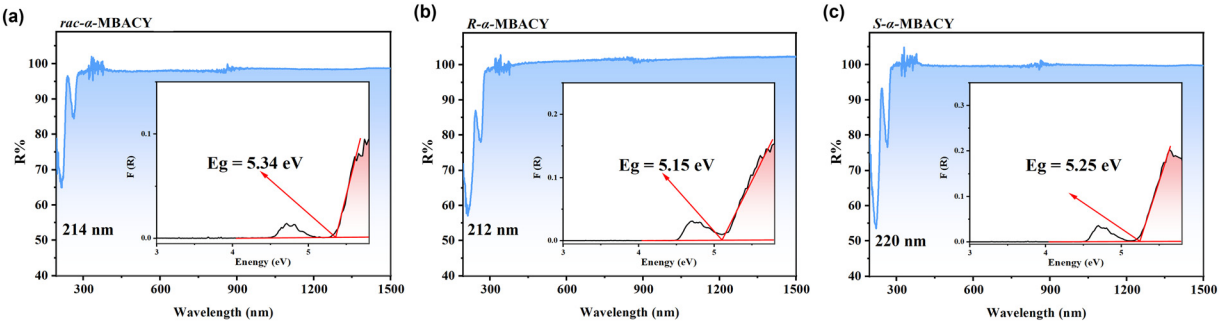

Fig. 4 The UV-vis-NIR diffuse reflectance spectra of *rac*-α-MBACY (a), *R*-α-MBACY (b) and *S*-α-MBACY (c).

MBACY and *S*-α-MBACY are the first reported metal-free cyanurates with SHG responses.

Birefringence measurements

The birefringence of *rac*-α-MBACY, *R*-α-MBACY and *S*-α-MBACY was measured by using polarizing microscopy (Fig. 5). The measured optical path differences for the three crystals are 1365.31 nm, 2835.75 nm and 7381.03 nm, respectively, with corresponding thicknesses of 10.95 μm, 8.76 μm and 23.92 μm. According to the formula $R = \Delta n \times d$, the experimental birefringence values of *rac*-α-MBACY, *R*-α-MBACY and *S*-α-MBACY at 546 nm are 0.125, 0.324 and 0.309, respectively. The experimental birefringence values of *R*-α-MBACY and *S*-α-MBACY are larger than those of many of the reported cyanurates, *e.g.* $KLi(HC_3N_3O_3)\cdot 2H_2O$ (Δn = 0.186@514 nm),[30] $Rb(H_3C_3N_3O_3)(NO_3)$ (Δn = 0.224@546.1 nm)[35] and $Cs_3Na(H_2C_3N_3O_3)_4\cdot 3H_2O$ (Δn = 0.29@514 nm),[36] so *R*-α-MBACY and *S*-α-MBACY are potential UV birefringent crystals.

Theoretical calculations

To further investigate the structure–property relationship of *rac*-α-MBACY, *R*-α-MBACY and *S*-α-MBACY, we performed first principles calculations based on density functional theory. As shown in Fig. S7,† the calculated band structure diagrams indicate that the band gaps of the three compounds are 4.00 eV, 4.32 eV and 4.32 eV respectively, which are indirect band gaps, and *R*-α-MBACY and *S*-α-MBACY exhibit the same band structure characteristics. The partial density of states diagram revealed that the valence band top and conduction band bottom of the three compounds are both composed of α-MBA cations with $(H_2C_3N_3O_3)^-$, which indicates that the large band gap of the three compounds is determined by both α-MBA cations and $(H_2C_3N_3O_3)^-$ (Fig. S8†). Due to the limitations of the GGA method, the calculated band gaps are all smaller than the experimental values. For a more accurate calculation of the birefringence, the scissor values of 1.34 eV, 0.83 eV, and 0.93 eV were used for *rac*-α-MBACY, *R*-α-MBACY and *S*-α-MBACY, respectively. As shown in Fig. 6, the calculated birefringence of *rac*-α-MBACY and *R*-α-MBACY at 546 nm is 0.113 and 0.344, respectively, which agree well with the experimental data. Meanwhile, the calculated birefringence of *S*-α-MBACY at 546 nm is 0.338, which is basically close to that of *R*-α-MBACY, indicating that the opposite chiral α-MBA cationic configuration does not change the birefringence magnitude of cyanurate. The integrated optical performances of *R*-α-MBACY and *S*-α-MBACY were quantified using the birefringent quality factor (BQF = $E_g \times \Delta n$),[66] and the results indicated that the BQF values of *R*-α-MBACY and *S*-α-MBACY exceeded those of most commercial birefringent crystals and cyanurates reported (Fig. 6d).

The electron localization function (ELF) map can be used to characterize the degree of the electron localization and can reflect the distribution of the electron cloud, allowing a qualitative examination of the anisotropy of the electron cloud in a crystal, which is closely related to the birefringence. From the ELF diagrams in Fig. 7, it can be observed that the electron density is primarily concentrated

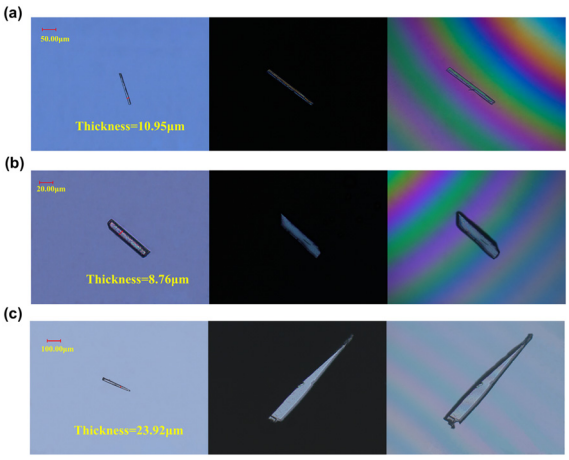

Fig. 5 Experimental birefringence at 546 nm for *rac*-α-MBACY (a), *R*-α-MBACY (b) and *S*-α-MBACY (c).

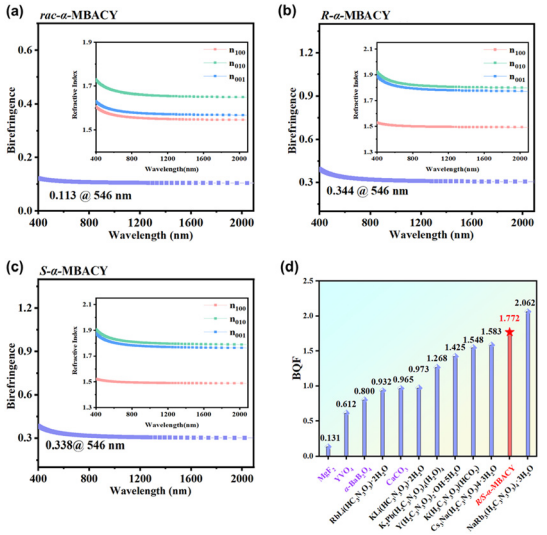

Fig. 6 The calculated birefringence of *rac*-α-MBACY (a), *R*-α-MBACY (b) and *S*-α-MBACY (c). Comparison of BQF values of some birefringent cyanurates and commercial birefringent crystals at 514–550 nm (d).

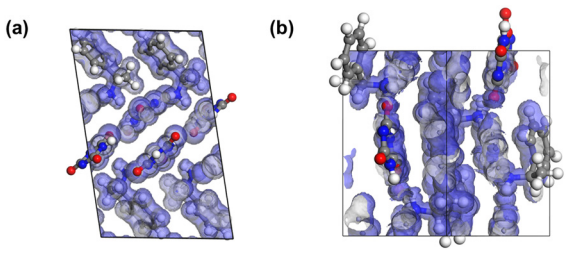

Fig. 7 The electron localization function diagrams of *rac*-α-MBACY (a) and *R*-α-MBACY (b).

within the planes of the $(H_2C_3N_3O_3)^-$ groups and the benzene rings, with a very sparse electron density distribution perpendicular to the planes. This great contrast highlights the pronounced anisotropy of the compounds. The dihedral angles between the intergroup electron clouds are smaller in *R*-α-MBACY than in *rac*-α-MBACY, which allows them to be nearly aligned along the same plane, favorable to produce large birefringence. Therefore, the large birefringence of *R*-α-MBACY originates from the favorable alignments of chiral α-MBA cations and $(H_2C_3N_3O_3)^-$ groups.

Conclusions

In conclusion, by adopting a chirality-driven approach, chiral cations were introduced into the cyanurate group system for the first time and three new birefringent materials with large band gaps, *rac*-α-MBACY, *R*-α-MBACY, and *S*-α-MBACY, were isolated. The existence of chirality dramatically decreases the dihedral angle between the α-MBA cation and $(H_2C_3N_3O_3)^-$ anion, producing three times enhancement of the birefringence. First principles calculations indicate that their birefringence properties originate from the favorable alignment of α-MBA cations and $(H_2C_3N_3O_3)^-$ groups. This work shows that the introduction of chiral organic cations is an effective route to explore new UV birefringent cyanurate crystals.

Data availability

Crystallographic data for this paper have been deposited at the CCDC under 2349919–2349921.

Author contributions

Yue Zhao: conceptualization, data curation, and visualization and writing – original draft; Chun-Li Hu: formal analysis; Peng-Fei Chen: writing – review & editing; Ming-Zhi Zhang: data curation; Jiang-Gao Mao: conceptualization, supervision, writing – review & editing and funding acquisition.

Conflicts of interest

There are no conflicts to declare.

Acknowledgements

This work was financially supported by the National Natural Science Foundation of China (No. 22375201, 22031009 and 21921001). The authors would like to thank Peng-Fei Li, Cheng-Shu Zhang, Hao-Yu Zhang, Jing-Hao Wei and Jia-Hang Wu of FJIRSM for helpful discussions on topics related to this work.

Notes and references

1 M. Cheng, W. Jin, Z. Yang and S. Pan, *Chem. Sci.*, 2022, **13**, 13482–13488.
2 G. Zou and K. M. Ok, *Chem. Sci.*, 2020, **11**, 5404–5409.
3 S. Ghosh, W. H. Wang, F. M. Mendoza, R. C. Myers, X. Li, N. Samarth, A. C. Gossard and D. D. Awschalom, *Nat. Mater.*, 2006, **5**, 261–264.
4 Z. Xie, L. Sun, G. Han and Z. Gu, *Adv. Mater.*, 2008, **20**, 3601–3604.
5 L. Zhang, D. Liang, Y. Wang, D. Li, J. Zhang, L. Wu, M. Feng, F. Yi, L. Xu, L. Lei, Q. Du and X. Tang, *Chem. Sci.*, 2018, **9**, 44–51.
6 L. H. Nicholls, F. J. Rodríguez-Fortuño, M. E. Nasir, R. M. Córdova-Castro, N. Olivier, G. A. Wurtz and A. V. Zayats, *Nat. Photonics*, 2017, **11**, 628–633.
7 X. Chen, W. Lu, J. Tang, Y. Zhang, Y. Wang, G. D. Scholes and H. Zhong, *Nat. Photonics*, 2021, **15**, 813–816.
8 X. Chen, W. Lu, J. Tang, Y. Zhang, Y. Wang, G. D. Scholes and H. Zhong, *Nat. Photonics*, 2021, **15**, 813–816.
9 Z. Guoqing, X. Jun, C. Xingda, Z. Heyu, W. Siting, X. Ke, D. Peizhen and G. Fuxi, *J. Cryst. Growth*, 1998, **191**, 517–519.
10 M. J. Dodge, *Appl. Opt.*, 1984, **23**, 1980.
11 L. G. DeShazer, in *Polarization Analysis and Measurement IV*, ed. D. H. Goldstein, D. B. Chenault, W. G. Egan and M. J. Duggin, SPIE, San Diego, CA, USA, 2002, vol. 4481, pp. 10–16.
12 Z. Liu, *Nature*, 2019, **574**, 394–398.
13 C. Hu, X. Cai, M. Wu, Z. Yang, J. Han and S. Pan, *Chem. Mater.*, 2022, **34**, 4224–4231.
14 L. Deng, M. Wu, Z. Yang, S. Han and S. Pan, *Inorg. Chem.*, 2022, **61**, 18238–18244.
15 Y. Yang, Y. Xiao, B. Li, Y.-G. Chen, P. Guo, B. Zhang and X.-M. Zhang, *J. Am. Chem. Soc.*, 2023, **145**, 22577–22583.
16 Y.-J. Jia, X. Zhang, Y.-G. Chen, X. Jiang, J.-N. Song, Z. Lin and X.-M. Zhang, *Inorg. Chem.*, 2022, **61**, 15368–15376.
17 Y. Kang and Q. Wu, *Coord. Chem. Rev.*, 2024, **498**, 215458.
18 P.-F. Li, C.-L. Hu, J.-G. Mao and F. Kong, *Coord. Chem. Rev.*, 2024, **517**, 216000.
19 X. Liu, L. Kang, P. Gong and Z. Lin, *Angew. Chem., Int. Ed.*, 2021, **60**, 13574–13578.
20 M. Mutailipu, M. Zhang, B. Zhang, L. Wang, Z. Yang, X. Zhou and S. Pan, *Angew. Chem., Int. Ed.*, 2018, **57**, 6095–6099.
21 G. Zou, H. Jo, S. Lim, T. You and K. M. Ok, *Angew. Chem., Int. Ed.*, 2018, **57**, 8619–8622.
22 G. Zou, Z. Lin, H. Zeng, H. Jo, S.-J. Lim, T.-S. You and K. M. Ok, *Chem. Sci.*, 2018, **9**, 8957–8961.
23 Y. Long, X. Dong, L. Huang, H. Zeng, Z. Lin and G. Zou, *Inorg. Chem.*, 2020, **59**, 12578–12585.
24 T. T. Tran, J. He, J. M. Rondinelli and P. S. Halasyamani, *J. Am. Chem. Soc.*, 2015, **137**, 10504–10507.
25 L. Huang, G. Zou, H. Cai, S. Wang, C. Lin and N. Ye, *J. Mater. Chem. C*, 2015, **3**, 5268–5274.
26 W. Zhang and P. S. Halasyamani, *CrystEngComm*, 2017, **19**, 4742–4748.
27 X. Dong, L. Huang, Q. Liu, H. Zeng, Z. Lin, D. Xu and G. Zou, *Chem. Commun.*, 2018, **54**, 5792–5795.
28 X. Liu, L. Kang, R. Guo and Z. Lin, *Dalton Trans.*, 2021, **50**, 17495–17498.
29 J. Lu, Y.-K. Lian, L. Xiong, Q.-R. Wu, M. Zhao, K.-X. Shi, L. Chen and L.-M. Wu, *J. Am. Chem. Soc.*, 2019, **141**, 16151–16159.

30 D. Lin, M. Luo, C. Lin, F. Xu and N. Ye, *J. Am. Chem. Soc.*, 2019, **141**, 3390–3394.
31 Y. Chen, C. Hu, Z. Fang and J. Mao, *Inorg. Chem.*, 2023, **62**, 2257–2265.
32 C. Yang, Y. Kang, X. Wang, J. Gou, Y. Xiong, Z. Zhu, L. Chen and Q. Wu, *Chem. Sci.*, 2024, **15**, 15725–15730.
33 M. Kalmutzki, M. Ströbele, F. Wackenhut, A. J. Meixner and H.-J. Meyer, *Angew. Chem., Int. Ed.*, 2014, **53**, 14260–14263.
34 F. Liang, L. Kang, X. Zhang, M.-H. Lee, Z. Lin and Y. Wu, *Cryst. Growth Des.*, 2017, **17**, 4015–4020.
35 X. Hao, M. Luo, C. Lin, G. Peng, T. Yan, D. Lin, L. Cao, X. Long, G. Yang and N. Ye, *Inorg. Chem.*, 2020, **59**, 10361–10367.
36 X. Meng, F. Liang, J. Tang, K. Kang, Q. Huang, W. Yin, Z. Lin and M. Xia, *Eur. J. Inorg. Chem.*, 2019, **2019**, 2791–2795.
37 J. Wang, X. Zhang, F. Liang, Z. Hu and Y. Wu, *Cryst. Growth Des.*, 2021, **21**, 7194–7200.
38 Y. Kuk, J. Kee and K. M. Ok, *Chem. – Eur. J.*, 2022, **28**, e202200007.
39 T. H. Moon, S.-J. Oh and K. M. Ok, *ACS Omega*, 2018, **3**, 17895–17903.
40 C. Yuan, X. Li, S. Semin, Y. Feng, T. Rasing and J. Xu, *Nano Lett.*, 2018, **18**, 5411–5417.
41 L. Yao, Z. Zeng, C. Cai, P. Xu, H. Gu, L. Gao, J. Han, X. Zhang, X. Wang, X. Wang, A. Pan, J. Wang, W. Liang, S. Liu, C. Chen and J. Tang, *J. Am. Chem. Soc.*, 2021, **143**, 16095–16104.
42 J. Cheng, G. Yi, Z. Zhang, Y. Long, L. Huang, H. Zeng, G. Zou and Z. Lin, *Angew. Chem., Int. Ed.*, 2023, **63**, e202318385.
43 J. Guan, Y. Zheng, P. Cheng, W. Han, X. Han, P. Wang, M. Xin, R. Shi, J. Xu and X.-H. Bu, *J. Am. Chem. Soc.*, 2023, **145**, 26833–26842.
44 J. Lee, J. B. Cho, Y. Li, K. Lee, J. I. Jang and K. M. Ok, *Small*, 2023, **20**, 2309323.
45 P. Cheng, X. Jia, S. Chai, G. Li, M. Xin, J. Guan, X. Han, W. Han, S. Zeng, Y. Zheng, J. Xu and X.-H. Bu, *Angew. Chem., Int. Ed.*, 2024, **63**, e202400644.
46 D. C. Marinescu and S. Tewari, *Phys. Rev. B*, 2023, **108**, 195303.
47 D. Fu, J. Xin, Y. He, S. Wu, X. Zhang, X. Zhang and J. Luo, *Angew. Chem., Int. Ed.*, 2021, **60**, 20021–20026.
48 A. Jung, Y. Li and K. M. Ok, *Dalton Trans.*, 2024, **53**, 105–114.
49 Y. Dang, X. Liu, B. Cao and X. Tao, *Matter*, 2021, **4**, 794–820.
50 X. Han, C. Chai, M. Jin, C. Fan and W. Zhang, *Adv. Opt. Mater.*, 2023, **11**, 2300580.
51 G. Long, R. Sabatini, M. I. Saidaminov, G. Lakhwani, A. Rasmita, X. Liu, E. H. Sargent and W. Gao, *Nat. Rev. Mater.*, 2020, **5**, 423–439.
52 O. V. Dolomanov, L. J. Bourhis, R. J. Gildea, J. A. K. Howard and H. Puschmann, *J. Appl. Crystallogr.*, 2009, **42**, 339–341.
53 G. M. Sheldrick, *Acta Crystallogr., Sect. A:Found. Adv.*, 2015, **71**, 3–8.
54 G. M. Sheldrick, *Acta Crystallogr., Sect. C:Struct. Chem.*, 2015, **71**, 3–8.
55 A. L. Spek, *J. Appl. Crystallogr.*, 2003, **36**, 7–13.
56 S. K. Kurtz and T. T. Perry, *J. Appl. Phys.*, 1968, **39**, 3798–3813.
57 V. Milman, B. Winkler, J. A. White, C. J. Pickard, M. C. Payne, E. V. Akhmatskaya and R. H. Nobes, *Int. J. Quantum Chem.*, 2000, **77**, 895–910.
58 J. P. Perdew, K. Burke and M. Ernzerhof, *Phys. Rev. Lett.*, 1996, **77**, 3865–3868.
59 M. D. Segall, P. J. D. Lindan, M. J. Probert, C. J. Pickard, P. J. Hasnip, S. J. Clark and M. C. Payne, *J. Phys.: Condens. Matter*, 2002, **14**, 2717–2744.
60 J. S. Lin, A. Qteish, M. C. Payne and V. Heine, *Phys. Rev. B: Condens. Matter Mater. Phys.*, 1993, **47**, 4174–4180.
61 H. G. Brittain, *Cryst. Growth Des.*, 2011, **11**, 2500–2509.
62 V. M. Chapela, M. J. Percino, A. Jiménez, R. Ortega-Martínez, C. A. Escalante and C. R. De Barbarín, *J. Mol. Struct.*, 2003, **648**, 115–124.
63 X. Meng, K. Kang, F. Liang, J. Tang, W. Yin, Z. Lin and M. Xia, *Inorg. Chem. Front.*, 2020, **7**, 3674–3686.
64 N. Wang, F. Liang, Y. Yang, S. Zhang and Z. Lin, *Dalton Trans.*, 2019, **48**, 2271–2274.
65 Y. Chen, C. Hu, Z. Fang, Y. Li and J. Mao, *Inorg. Chem.*, 2022, **61**, 1778–1786.
66 Y. Zhao, L. Zhu, Y. Li, X. Kuang, J. Luo and S. Zhao, *Mater. Chem. Front.*, 2023, **7**, 3986–3993.